RSC Advances

PAPER

View Article Online
View Journal | View Issue

Cite this: *RSC Adv.*, 2015, **5**, 68542

Effect of LiCl presence on the hydrogen storage performance of the $Mg(NH_2)_2$–2LiH composite†

N. S. Gamba,*[ab] P. Arneodo Larochette[abc] and F. C. Gennari[abc]

Received 25th June 2015
Accepted 6th August 2015

DOI: 10.1039/c5ra12241d

www.rsc.org/advances

The $Mg(NH_2)_2$–2LiH composite is a promising hydrogen storage material due to its favourable thermodynamics and hydrogen storage reversibility. However, its application is restricted owing to the presence of severe kinetic barriers. In the present work, the $Mg(NH_2)_2$–2LiH was synthesized by metathesis reaction of $LiNH_2$ plus $MgCl_2$ and posterior milling with LiH. LiCl is a co-product that operates as a separation phase favouring the nanostructure of the composite. The synthesized material exhibits good dehydrogenation rate and approximately the theoretical hydrogen storage capacity at 200 °C. However, the formation of $Li_4(NH_2)_3Cl$ and the incomplete rehydrogenation of $Li_2Mg_2(NH_2)_3$ are progressively favoured during successive hydrogen cycling, deteriorating the storage properties. Two competitive reactions can simultaneously occur involving $LiNH_2$ as an intermediate phase: the formation of $Li_4(NH_2)_3Cl$ using the co-product LiCl and the complete dehydrogenation of $Li_2Mg_2(NH_2)_3$ leading to the $Li_2Mg(NH)_2$ formation. The worst effect of $Li_4(NH_2)_3Cl$ formation was simultaneously demonstrated by kinetics and PCI measurements. The amide-chloride phase was actually the active species for the deterioration of dehydrogenation kinetics and hydrogen storage capacity of the Li–Mg–N–H–Cl system.

1. Introduction

Solid-state hydrogen storage materials are one of the most important subjects under development to allow the practical use of hydrogen-fuelled vehicles. Light element complex hydrides such as alanates, borohydrides and amides are considered as promising materials for safe and efficient hydrogen storage.[1–7] However, all known hydrides are inadequate for hydrogen storage applications due to one or more limitations, such as unfavourable thermodynamics, poor kinetics, inability to rehydrogenate or low reversible hydrogen storage capacity.[8–10]

In spite of these drawbacks, solid-state hydrogen storage in metal–N–H systems has been extensively investigated in the last years as a result of their promising thermodynamic stability and the viability of reversible storage. Several studies of the Li–Mg–N–H system with different compositions or different starting materials have been reported since 2004.[2,3,11–16] By varying the molar ratio of $Mg(NH_2)_2$ and LiH, Hu *et al.* found that the optimum LiH : $Mg(NH_2)_2$ molar ratio was 2. They observed that if the molar ratio was below 2, ammonia generation during dehydrogenation occurred, and if the molar ratio was above 2, a reduction in hydrogen storage efficiency was observed.[13] Compared with the Li–N–H system, Li–Mg–N–H system demonstrates much lower absorption and desorption temperatures and higher hydrogen desorption pressures, while the total reversible capacity is still quite high.[2,3] In addition, the thermodynamics is favourable, with a reaction heat of 44.1 kJ mol^{-1} H_2.[17] Therefore, the Li–Mg–N–H system became to be considered one of the strongest candidates for hydrogen storage materials, according with the following reaction:

$$Mg(NH_2)_2 + 2LiH \leftrightarrow Li_2Mg(NH)_2 + 2H_2 \quad (1)$$

Numerous studies have analysed the reversible reaction mechanism of the Li–Mg–N–H system.[3,17–19] Chen *et al.* showed that the ammonia-mediated mechanism is energetically unfavorable.[20] Isothermal and non-isothermal kinetic measurements of the chemical reaction (1) as well as the thermal decomposition of $Mg(NH_2)_2$ revealed that the route by thermal decomposition is unlikely to be an elementary step in the chemical reaction of $Mg(NH_2)_2$ and LiH. Hydrogen desorption of the $Mg(NH_2)_2$–2LiH composite occurs in a two-step reaction, which results in the intermediate phase $Li_2Mg_2(NH)_3$, according to reactions (2) and (3).[21]

$$2Mg(NH_2)_2 + 3LiH \rightarrow Li_2Mg_2(NH)_3 + LiNH_2 + 3H_2 \quad (2)$$

$$Li_2Mg_2(NH)_3 + LiNH_2 + LiH \rightarrow 2Li_2Mg(NH)_2 + H_2 \quad (3)$$

Although the predicted dehydrogenation temperature of $Mg(NH_2)_2$–2LiH is below 90 °C at 1 bar H_2 pressure,[17] this

[a]*Consejo Nacional de Investigaciones Científicas y Técnicas (CONICET), Av. Bustillo 9500, R8402AGP, S. C. de Bariloche, Río Negro, Argentina. E-mail: gamba.nadia@gmail.com; Fax: +54 294 4445190; Tel: +54 294 4445712*

[b]*Centro Atómico Bariloche (CNEA), Argentina*

[c]*Instituto Balseiro, Universidad Nacional de Cuyo, Argentina*

† Electronic supplementary information (ESI) available. See DOI: 10.1039/c5ra12241d

composite displays reversible hydrogen storage (5.5% wt H_2) at a temperature above 180 °C, attributable to the existence of a kinetic barrier.[20] Kinetic studies revealed that the rate-limiting step for the dehydrogenation process of $Li_2Mg(NH)_2$ was controlled by diffusion.[22] Thus, the direction to the investigations to enhance the desorption kinetics of this hydrogen storage system should be: (a) the use of nanomaterial to the reduction of the diffusion distance,[22,23] (b) the milling of high energy to introduce lattice defects and increase the diffusion coefficient,[24] and/or (c) doping to increase the lattice distortion and thus the diffusion rate.[22]

One strategy to overcome the kinetic barrier is the doping of the Li–Mg–N–H system using metal hydrides and halides, among others.[25–27,29–37] Potassium hydride showed to be an effective additive that can reduce the desorption temperature by favouring a metathesis reaction between KF and LiH. The reversible hydrogen release and uptake of the $Mg(NH_2)_2$–2LiH composite can be carried out at a lower temperature than the sample without the dopant.[25–27] Furthermore, it was found that metal halides play a role to decrease the operating temperature and improve the hydrogen storage kinetics, in particular the potassium halides.[27,28] Although only samples with KF showed a thermodynamic destabilization and kinetic improvement in the hydrogen storage reaction due to the presence of KH, other potassium halides (KCl, KBr, and KI) remained almost unchanged.[29] Recently, Anderson *et al.* investigated the reaction of lithium amide and lithium imides with lithium or magnesium chlorides, bromides and iodides, which resulted in a series of amide-halide and imides-halide phases.[31,35,36] These amide-halide phases were synthesized by heating lithium amide and LiH or MgH_2 with the appropriate halides.[31] The incorporation of lithium/magnesium halides into lithium amide enhanced the hydrogen storage properties of the $LiNH_2$–LiH composite and promoted the reduction/elimination of the ammonia as a product. Moreover, it was found that there is a correlation between the conductivity and the hydrogen storage properties: if the conductivity of lithium ions is improved, it might lead to faster dehydrogenation kinetics.[31–35]

In a further study, Leng *et al.* investigated the effect of $MgCl_2$ on the hydrogen desorption properties of the Li–N–H system.[30] Their research showed that the desorption properties can be significantly improved by the addition of $MgCl_2$ although the result depended on the $MgCl_2$ amount. Three different mechanisms were proposed to explain the effects of $MgCl_2$ with different quantities in this system. With small amount (<4 mol%), $MgCl_2$ can improve the hydrogen storage properties as a trap of NH_3, and with more quantities of $MgCl_2$, Mg^{2+} can dissolve into $LiNH_2$ to give a solid solution. While greater amounts of $MgCl_2$ (>25 mol%) are added, the Li–N–H system turns into a Li–Mg–N–H system through the reaction between $MgCl_2$ and $LiNH_2$, which can lead to the improvement of the hydrogen desorption temperature promoting the decomposition of $LiNH_2$. In a recent work, we showed that the ball mixing of $AlCl_3$ (0.03 mol) with $LiNH_2$–1.6LiH improved the hydrogen storage properties of the Li–N–H system, with practically a complete suppression of NH_3 emission.[37] In fact, a stable hydrogen storage capacity of about 4.5–5.0 wt% is observed under cycling and it is completely desorbed in 30 min at 275 °C. It was demonstrated that the inclusion of Al^{3+} in the $LiNH_2$ structure modifies the thermodynamic properties of the $LiNH_2$–LiH sample, which could be the main cause of the enhancement of the hydrogen sorption behaviour observed.

Further investigations also evidenced the effect of the halides on the properties of the Li–N–H system:[33,34] it was found that Br halides had a positive effect, while Cl halides did not show significant improvements. In fact, the addition of LiBr induced *in situ* formation of a $Li_7(NH_2)_6Br$ phase, which weakens the N–H bond and also promotes the migration of Li^+, with the consequent improvement of the dehydrogenation kinetics of the Li–Mg–N–H system. In the case of the LiCl addition, a more complex dehydrogenation process was observed with respect to the undoped sample, although the onset temperature of dehydrogenation remained almost the same. Nevertheless, there is still no clear understanding of the behaviour of the halides, in particular chlorides, on the hydrogen storage properties of the Li–Mg–N–H system.

In this study, we have investigated the dehydrogenation properties of the $Mg(NH_2)_2$–2LiH–2LiCl composite and further analysed the effect of the LiCl on the hydrogen storage properties. For this purpose, $Mg(NH_2)_2$ was synthesized, since it is not commercially available, by a novel method of metathesis reaction activated by milling where LiCl is obtained as a co-product. The synthesis conditions of $Mg(NH_2)_2$, its dehydrogenation kinetics and the structural, microstructural and thermal studies of the composites before and after dehydrogenation cycles are studied. The effect of the $Li_4(NH_2)_3Cl$ formation during hydrogen cycling on the hydrogen storage properties of the Li–Mg–N–H–Cl was clarified.

2. Experimental details

2.1. Starting materials and sample synthesis

$LiNH_2$ (Sigma-Aldrich, purity ≥ 98%) and anhydrous $MgCl_2$ (Sigma-Aldrich, purity ≥ 98%) powders in a molar ratio of 2 : 1 were milled in a Fritsch P6 planetary mill under a 0.1 MPa of argon atmosphere at 400 rpm (ball-to powder ratio of 60 : 1). The total time of the milling was determined on the basis of the final product formed. The sample obtained was indicated as MN-*X*, where *X* denotes the milling time. To avoid temperature ramping during milling, there was a 15 minute pause for each 10 minute run. The as-milled MN sample was then mixed with LiH (Sigma-Aldrich, purity ≥ 95%). The composite was prepared by milling in a 1 : 2 molar ratio at 400 rpm for additional time under 0.1 MPa of Ar. The obtained samples were named MNLH-*X*, where *X* denotes the milling time. The sample MNLH-*X* submitted to thermal treatment at 200 °C for 0.5 h and 6.0 MPa of hydrogen pressure was indicated as MNLH-*X*tt.

For comparison purpose, $Li_4(NH_2)_3Cl$ was synthesized according with Anderson *et al.*,[31] using $LiNH_2$ and LiCl (Sigma-Aldrich, purity ≥ 99%) as starting materials in the 1 : 4 ratio. The sample was then mixed with LiH by milling in a 1 : 3 molar ratio at 400 rpm under 0.1 MPa of Ar. The final composite was named as LCLH. On the other hand, the as-prepared LCLH was heated at 200 °C for 0.5 h under 6.0 MPa of H_2 and indicated as

LCLH-tt. The final material is a mixture of cubic and hexagonal $Li_4(NH_2)_3Cl$ phases (see Fig. S1†).[31]

All handling of the samples, before and after milling, were performed under an inert atmosphere of high purity argon in a MBraun Unilab glove box with a circulative purification system. Oxygen and moisture levels were kept below 1 ppm during all operations to avoid degradation of the samples.

2.2. Sample characterization

Structural information of the different samples was obtained by means of X-ray powder diffraction analysis (XRPD, Philips PW 1710/01 Instruments) and by Fourier transform infrared spectroscopy (FTIR, Perkin Elmer Spectrum 400). The PXRD measurements were performed with CuKα radiation (graphite monochromator, voltage of 40 kV and a current of 30 mA) in a range of $2\theta = 10°–80°$ with a step size of 0.02° and 3 seconds for each step. During the PXRD data collection all the samples were maintained under Ar atmosphere using a tightly sealed sample holder to prevent the reaction between samples with oxygen and humidity. The crystallite sizes of $Mg(NH_2)_2$ and LiCl were determined by the Scherrer equation, using the most intense peak of each phase. The IR spectra were obtained at room temperature in the 800–4000 cm^{-1} wavenumber range. The powders were pressed into pellets with dry KBr and put in a specially designed cell to prevent the reaction between samples with air and closed in the glove box. The gases released during dehydrogenation of the as-milled and as-cycled mixtures were collected in a degassed quartz optical cell with KBr windows and gas phase spectra at room temperature were taken. No NH_3 emission was detected by gas-FTIR analysis during sample decomposition up to 200 °C.

Textural measurements were performed at liquid nitrogen temperature to determine the specific surface area (SSA) based on the Brunauer–Emmett–Teller (BET) method using Micromeritics ASAP 2020 instrument.

The thermal behaviour of the samples was studied by differential scanning calorimetry analysis (DSC, TA 2910 calorimeter) under argon atmosphere, with a flow rate of 122 ml min^{-1} and a heating rate of 5 °C min^{-1} for routine analysis. For DSC thermal analysis about 3–5 mg of samples were loaded into aluminium capsules and closed in the argon-filled glove box to minimize the exposure of the powder to air. The Kissinger method[38] was employed to determine the activation energy of the dehydrogenation process, according to the following equation:

$$\frac{d\left[\ln\left(\frac{\beta}{T_p^2}\right)\right]}{d\left(\frac{1}{T_p}\right)} = \frac{-E_{app}}{R} \quad (4)$$

where T_p is the peak temperature of the endothermic event, β is the heating rate, E_{app} is the apparent activation energy and R is the ideal gas constant. The slope of the fitted line corresponds to the activation energy (E_{app}) of the reaction. The T_p was obtained from the DSC curves at heating rates of 1, 2, 5, 10 and 15 °C min^{-1}.

SEM observations with secondary electrons and EDS analyses were carried out in an electron scanning microscope SEM – Nova Nano SEM 230. To minimize the exposition to air and moisture, the as-milled and as-cycled (8^{th} cycle) MNLH-5 samples were prepared under argon in the glove box and placed inside a glass vial. Samples were transferred from the glass vial to the SEM facility, reducing the air exposure time to less than 30 seconds.

Pressure composition isotherm (PCI) curves, hydrogen sorption kinetics and desorption–absorption capacities were obtained using a modified Sieverts-type device, coupled with a mass flow controller. A known mass sample is transferred in the glove box into a stainless steel reactor, which is then connected to the Sieverts apparatus. For hydrogen desorption PCI measurement, a programmed amount of hydrogen is extracted from the system using the mass flow controller, so pressure decreases. The criteria used to determine if the system reaches the equilibrium condition are: if the temporal variation of pressure is lower than a fixed value or to wait for a selected time. When one of these criteria is reached, it is considered that the system is in equilibrium and a point in the PCI curve is saved. Then, the software starts the following equilibrium point using again the mass flow controller.

The dehydrogenation experiments were measured under isothermal conditions at 200 °C and 0.02 MPa of hydrogen pressure. Before each dehydrogenation measurement, the sample was heated up to the reaction temperature under hydrogen pressure (6.0 MPa) and kept at this temperature for 30 min before hydrogen desorption. The rehydrogenation process was performed with a hydrogen pressure of 6.0 MPa, which was kept approximately constant using a mass flow controller during the 2 h of measuring time. In addition, non-isothermal dehydrogenation experiments were conducted from 20 to 300 °C with constant heating rates of 5 °C min^{-1} and 0.02 MPa of hydrogen. The amount of absorbed/desorbed hydrogen is reported as wt% with respect to the total hydrided mass, excluding LiCl mass.

3. Results and discussion

3.1 Synthesis of $Mg(NH_2)_2$ – 2LiH–2LiCl composite from $MgCl_2$ and $LiNH_2$

$Mg(NH_2)_2$ was synthesized by milling of $2LiNH_2$ and $MgCl_2$ for 2 and 5 hours to ensure the complete consumption of the starting materials. The XRPD patterns of MN-2 and MN-5 are similar and only that corresponding to 5 h is shown in Fig. 1(a). The complete absence of any diffraction peaks from $LiNH_2$ and $MgCl_2$ starting materials was observed and LiCl is the only crystalline phase detected. Fig. 1(b) shows the FTIR spectra of the MN-2 and MN-5 samples after milling. As a reference, $LiNH_2$ spectrum of the starting material is shown. Analysis of MN-2 and MN-5 FTIR spectra confirms the formation of $Mg(NH_2)_2$ by the observation of the main bands at 3273 cm^{-1} and 3327 cm^{-1}.[39] However, due to the width of the FTIR bands, it is not discarded the presence of minor amount of $LiNH_2$ (3313 and 3259 cm^{-1} bands) by comparison with the reference spectrum. Then, the ball milling induces a metathesis reaction,

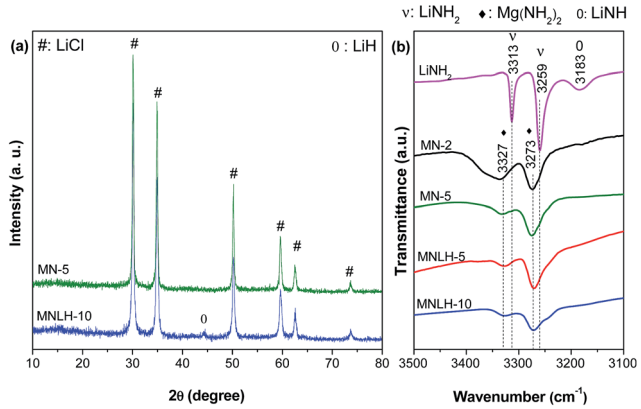

Fig. 1 (a) XRPD patterns of the MN-5 and MNLH-10 samples. (b) FTIR spectra of the NM-2, MN-5, MNLH-5 and MNLH-10 samples. The spectrum of $LiNH_2$ is shown as reference.

which results principally in the formation of $Mg(NH_2)_2$ and LiCl, according to eqn (5):

$$2LiNH_2 + MgCl_2 \rightarrow Mg(NH_2)_2 + 2LiCl \quad (5)$$

It was demonstrated that this type of mechanochemical process allows the production of nanoparticles. In addition, the presence of a buffer phase could act as dispersing agent avoiding agglomeration.[40]

As a following step, LiH was added to MN-2 and MN-5 by additional milling for 3 h and 5 h respectively, for the production of MNLH-5 and MNLH-10 composites. Fig. 1(a) displays the XRD diffraction pattern of MNLH-10, which looks similar to that of MNLH-5 (not shown). Clearly, the peaks corresponding to LiCl and LiH phases are identified, suggesting that the addition of LiH does not introduce additional interaction between reactants. The crystallite sizes of LiCl and LiH phases are 25 nm and 16 nm, respectively. The final phases in the composites (MNLH-5 and MNLH-10) were also analysed by FTIR (Fig. 1(b)), where $Mg(NH_2)_2$ characteristic signals at 3273 cm^{-1} and 3327 cm^{-1} were observed.[39] Similarly to MN-2 and MN-5, the presence of minor amount of $LiNH_2$ cannot be discarded. Although FTIR confirms the formation of $Mg(NH_2)_2$, no diffraction peaks from this phase were detected, which is due to the poor crystallinity and/or the nanometre grain size of $Mg(NH_2)_2$ phase.

Considering that similar structural phases were obtained after 5 h (MNLH-5) and 10 h (MNLH-10) of milling, we selected the material involving the minimum milling time (5 h) for further studies. This short time is enough to allow the formation of $Mg(NH_2)_2$ and helps to avoid possible contamination caused by the milling chamber and balls.

3.2 Dehydrogenation properties of $Mg(NH_2)_2$–2LiH–2LiCl composite

To analyse the dehydrogenation kinetics of the MNLH-5 composite, the de/rehydrogenation cycles were measured under isothermal conditions. Fig. 2(a) displays the

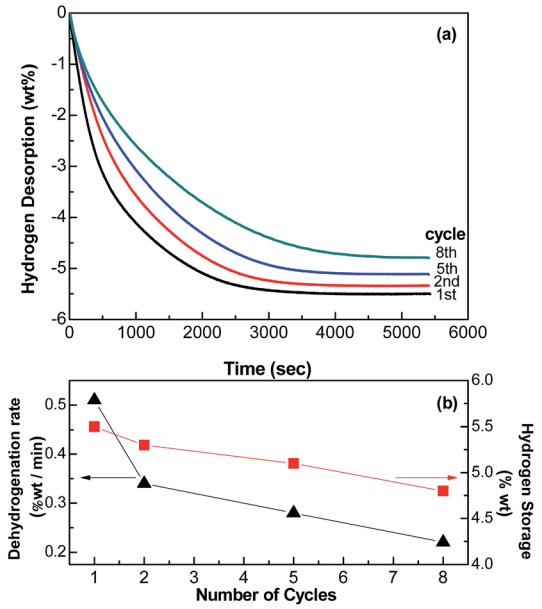

Fig. 2 (a) Hydrogen desorption curves of the MNLH-5tt sample at 200 °C at 0.02 MPa of hydrogen pressure. (b) Dehydrogenation rate and hydrogen storage capacities of the different cycles.

dehydrogenation curves of MNLH-5tt cycled sample at 200 °C under 0.02 MPa of hydrogen. All cycles showed similar hydrogen desorption behaviour although the dehydrogenation rates and the storage capacity decreased. Fig. 2(b) shows the dehydrogenation rate and the hydrogen storage capacity with the cycling. Taking the slope between 0.02 wt% and 0.15 wt% as a function of time, it was obtained a dehydrogenation rate of 0.51 wt% min^{-1} for the 1st cycle in comparison with 0.22 wt% min^{-1} for the 8th cycle. On the other hand, the hydrogen storage for the 8th cycle was 13% lower than the initial capacity obtained for the first cycle (5.4 wt%). To understand the observed kinetic performance of the MNLH-5tt composite, several studies of the samples in different stages of the hydrogen cycling were performed.

3.3 Structural and microstructural studies of $Mg(NH_2)_2$–2LiH–2LiCl composite before and after de/hydrogenation cycles

To study the structural changes that occur during heating, before and after hydrogen cycling, the combination of XRPD and FTIR techniques were used (Fig. 3). Before the first dehydrogenation, the MNLH-5 composite was heated under 6.0 MPa of hydrogen at the selected temperature (200 °C) and kept to this temperature for 30 min (named MNLH-5tt). This sample is more representative of the initial state of the composite before the first dehydrogenation cycle.

In Fig. 3(a), the most intense peaks corresponding to the $Mg(NH_2)_2$ phase can be easily seen, which indicates an increment in the crystallinity of the MNLH-5tt composite in relation to the as-milled MNLH-5 (Fig. 1(a)). In addition, the diffraction peaks of LiCl co-product and LiH are also identified. After the first dehydrogenation cycle, crystallite sizes of $Mg(NH_2)_2$, LiCl

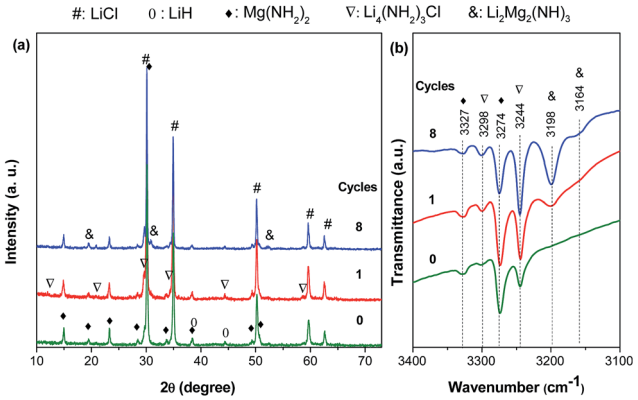

Fig. 3 (a) XRPD patterns and (b) FTIR spectra of the MNLH-5tt (cycle 0) and MNLH-5tt samples (1st and 8th rehydrogenation cycles).

and LiH are 40, 34 and 27 nm, respectively, which show a slight increment with respect to the as-milled sample. In Fig. 3(b) the vibration of the N–H bond at 3274 and 3328 cm^{-1} confirms the presence of $Mg(NH_2)_2$. However, other signals at 3298 and 3344 cm^{-1} appeared, which could not be easily assigned as corresponding to Li or Mg amides reported in literature. These bands progressively increase with the cycling and are clearly identified by FTIR after the 1st and 8th rehydrogenation cycles (Fig. 3(b)). Simultaneously, in the XRPD patterns after cycling, new incipient peaks at $2\theta = 11.9°$, $20.8°$, $29.8°$ and $34.6°$ appeared (Fig. 3(a)). Moreover, as evidence of uncompleted rehydrogenation, the band at 3198 cm^{-1} associated with $Li_2Mg_2(NH)_3$ phase is detected.[41,42] In particular, strong evidence of the uncompleted rehydrogenation is obtained for the MNLH-5 after 8th cycle. From XRPD pattern (Fig. 3(a)) the presence of the main peak of $Li_2Mg_2(NH)_3$ at $2\theta = 30.8°$ was detected as the minority phase,[43] whereas from FTIR (Fig. 3(b)) the bands at 3198 cm^{-1} and 3164 cm^{-1} associated to the $Li_2Mg_2(NH)_3$ phase were also observed, which corresponds to an intermediate phase of the overall reaction (1).[41] In addition, the crystallite size for $Mg(NH_2)_2$ phase remains practically constant from the 1st to 8th cycles (40 nm). Moreover, slight changes were observed for the BET area values: from 8 $m^2\ g^{-1}$ to 6 $m^2\ g^{-1}$ for as-milled and as-8th cycled samples.

According to these results, the $Mg(NH_2)_2$ and $Li_2Mg_2(NH)_3$ phases are obtained simultaneously with a new unidentified phase during hydrogen cycling. This new phase has FTIR bands at 3298 and 3344 cm^{-1} with intensities increasing with hydrogen cycling. These bands seem similar to those previously reported using Raman spectroscopy for $Li_4(NH_2)_3Cl$ and $Li_3Mg_{0.5}(NH_2)_3Cl$.[31] However, due to the fact that their specific positions were not reported, the comparison with our FTIR spectra is difficult. By inspection of the Raman reported data, the strongest band in the Raman spectra for $Li_4(NH_2)_3Cl$ and $Li_3Mg_{0.5}(NH_2)_3Cl$ seems to be in the same position ($\sim$3240 cm^{-1}), *i.e.* there was no evident shift due to Mg incorporation. The other band looked at $\sim$3300 cm^{-1} for $Li_4(NH_2)_3Cl$, while for $Li_3Mg_{0.5}(NH_2)_3Cl$ phase showed a slight shift at $\sim$3270 cm^{-1}.[31] On the other hand, a recent work on the addition of different lithium halides to $Mg(NH_2)_2$–2LiH confirms the formation of $Li_4(NH_2)_3Cl$ phase by the presence of FTIR band at 3303 cm^{-1}.[34] In our case, the identification of the band at 3298 cm^{-1} and 3244 cm^{-1} is more representative of $Li_4(NH_2)_3Cl$ phase than $Li_3Mg_{0.5}(NH_2)_3Cl$. However, some type of Mg substitution in the amide-chloride structure cannot be ruled out. Therefore, $Li_4(NH_2)_3Cl$ phase was progressively formed as consequence of cycling.

To examine the morphologies, SEM images of the as-milled and as-cycled MNLH-5 samples are shown in Fig. 4(a) and (b), respectively. In general, there is not an organized microstructure. The particles of the as-milled sample look irregular in shape and size, with some type of agglomeration. The size of most part of the particles is larger than 500 nm (Fig. 4(a)). Similar non-uniform shape and size of the particles was found for the cycled sample, both of which are interconnected with each other. Several EDS analyses performed on different zones of 1 μm × 1 μm give an average Mg : Cl molar ratio equal to 1 : 2, in agreement with the theoretical composition. Previous studies[20,23,24] have shown the influence of the microstructure of $Mg(NH_2)_2$–2LiH sample on the dehydrogenation rate or the temperature onset for dehydrogenation. Samples with larger particle size showed poorer contact between reactants, which depletes the direct interaction of $Mg(NH_2)_2$ with 2LiH and increases the distances for mass transport. Since a clear increase in the particle size or agglomeration for the as-cycled sample was not observed by comparison with the as-milled sample, the reduction of both hydrogen storage capacity and dehydrogenation rate with cycling (Fig. 2) does not seem to be related with microstructural changes. In fact, the crystallite size for $Mg(NH_2)_2$ phase remains practically constant from the 1st to the 8th cycles (40 nm). On the other hand, although the crystallite sizes of LiCl and LiH increase slightly after the 8th cycle, they continue to be within the nanometre range. These results reinforce the idea that LiCl could acts as dispersing agent, avoiding agglomeration.[40,44] Then, the experimental evidence suggests that the deterioration of the hydrogen storage performance of MNLH-5 is associated with structural changes more than with microstructural ones.

3.4 Kinetic studies of $Mg(NH_2)_2$–2LiH–2LiCl composite

To correlate the structural changes observed with the thermal stability of the samples, dehydrogenation studies were performed using the DSC technique. Fig. 5 shows DSC curves of the

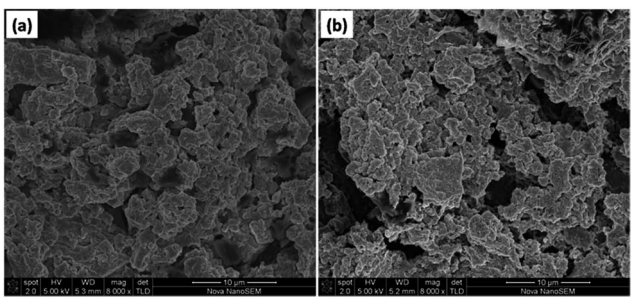

Fig. 4 SEM images of MNLH-5 sample (a) as-milled and (b) after the 8th cycle of rehydrogenation.

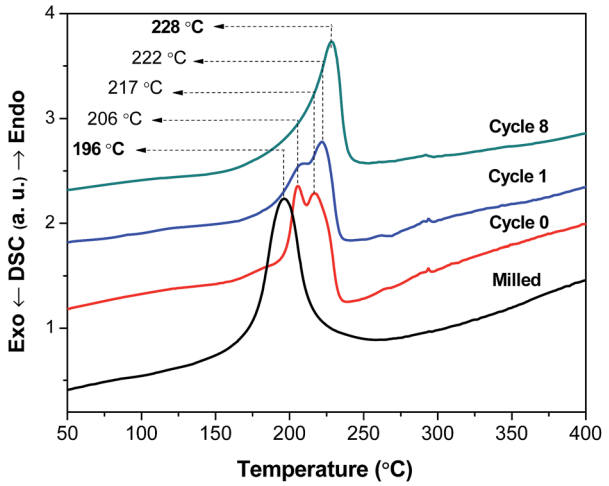

Fig. 5 DSC curves of as-milled MNLH-5, MNLH-5tt, MNLH-5 after the 1st and the 8th rehydrogenation cycles. Heating ramp of 5 °C min^{-1}, argon flow 122 ml min^{-1}.

as-milled and as-cycled samples. DSC curves for MNLH-5 exhibit a single endothermic event centered at 196 °C, involving hydrogen desorption from as-milled $Mg(NH_2)_2$–2LiH–2LiCl. In the case of MNLH-5tt (cycle 0), the DSC curve shows two endothermic events, with the maximum shifted to higher temperatures. The first one at 206 °C could be mainly related with the dehydrogenation of $Mg(NH_2)_2$–2LiH–2LiCl by similarities with the as-milled sample; while the second one at 217 °C could be influenced for the thermal decomposition of $Li_4(NH_2)_3Cl$, the secondary phase observed by XRPD and FTIR (Fig. 3(a) and (b)). Similar behaviour was observed for the MNLH-5 sample after the 1st dehydrogenation cycle. In the case of 8th cycle, only one peak is identified and it is shifted to higher temperature. By comparison, thermal treated and cycled samples do not share the same starting temperature as the as-milled material, suggesting a negative effect on the dehydrogenation kinetics for the MNLH-5 containing $Li_4(NH_2)_3Cl$ phase.

To reinforce previous interpretation, dehydrogenation activation energies (E_{pp}) for the as-milled and as-cycled (1st and 8th cycles) samples were determined using the Kissinger method (Fig. 6). The Fig. 6(a) shows the dependency of $\ln(\beta/T_p^2)$ with $1/T_p$, according to the Kissinger method. The slope of the fitted line was used to determine the value of E_{app}/R. The DSC technique was applied to collect the maximum reaction rate temperatures at various heating rates (1, 2, 3, 5, and 15 °C min^{-1}). The DSC curves measured to construct Kissinger plot are shown in Fig. 6(b). The activation energies obtained for hydrogen desorption are 132 ± 4 kJ mol^{-1}, 123 ± 6, 150 ± 1 and 142 ± 6 kJ mol^{-1} (correlation coefficient $R^2 = 0.99$) for MNLH-5, 1st cycle-MNLH peak (1), 1st cycle-MNLH peak (2) and 8th cycle-MNLH, respectively. These values of activation energies are of similar order; however, for the cycle 8, an increment in the activation energy of about 8% was observed in comparison with the as-milled MNLH-5 sample. This negative effect could be consequence of the progressive formation of the amide-chloride observed during cycling (Fig. 3(b)).

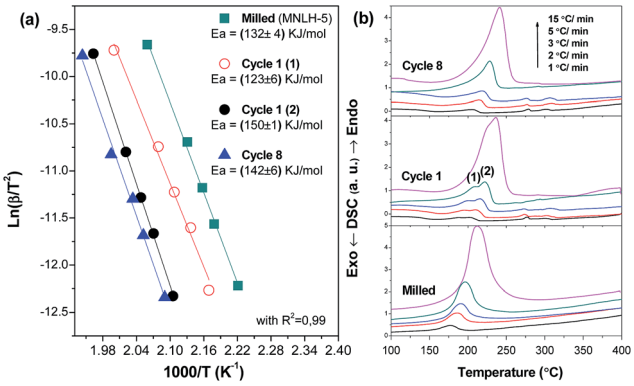

Fig. 6 (a) Kissinger plot (b) DSC curves for MNLH-5, 1st cycle-MNLH and 8th cycle-MNLH samples. The first and second peaks are denoted as (1) and (2), respectively.

3.5 Comparison of the $Mg(NH_2)_2$–2LiH–2LiCl and $Li_4(NH_2)_3Cl$–3LiH

Dehydrogenation studies under non-isothermal and isothermal conditions were performed for the MNLH-5, MNLH-5tt and LCLH-tt to clarify the influence of the $Li_4(NH_2)_3Cl$ formation on the hydrogen desorption kinetics (Fig. 2(a)). Non-isothermal dehydrogenation was measured to determine the starting temperature of hydrogen release for the amide-chloride phase. Fig. 7(a) displays the dehydrogenation curves of MNLH and MNLH-5tt, which consist in $Mg(NH_2)_2$–2LiH–LiCl and $Mg(NH_2)_2$–$Li_4(NH_2)_3Cl$–3LiH–LiCl mixtures, respectively. Dehydrogenation starts at ~195 °C and reaches about 3.5 wt% of hydrogen released to 230 °C and 240 °C for MNLH-5 and MNLH-5tt, respectively.

Complete dehydrogenation is reached for both samples at 260 °C. Similar behaviour was obtained from DSC curves (Fig. 4), where a faster hydrogen release is observed for MNLH-5 with respect to MNLH-5tt. A single cubic $Li_2Mg(NH)_2$ phase was produced after the dehydrogenation to 300 °C (see Fig. S2†). Alternatively, dehydrogenation from the LCLH-tt sample starts at about 245 °C, with a total of 3.0 wt% of hydrogen at 300 °C.

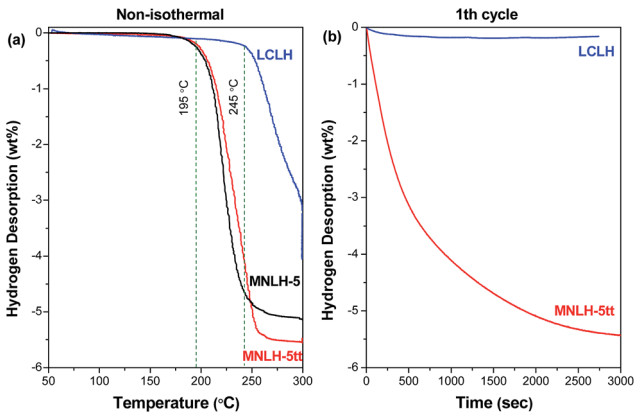

Fig. 7 (a) Non-isothermal hydrogen desorption of the samples MNLH-5, MNLH-5tt and LCLH-tt (b) isothermal hydrogen desorption at 200 °C of the samples with heat treatment MNLH-5tt and LCLH-tt.

Additional time at 300 °C or higher temperatures would be needed for a complete dehydrogenation (see Fig. S2†). By fitting the linear part of the dehydrogenation curves, the hydrogen desorption rates for MNLH-5 and MNLH-5tt composites were estimated at about 0.14 and 0.11H_2 wt% min^{-1}, respectively, which is greater in relation to the LCLH-tt composite (0.05H_2 wt% min^{-1}). Clearly, the presence of $Li_4(NH_2)_3Cl$ not only retards the beginning of the hydrogen releasing but also decreases the dehydrogenation rate.

In addition, isothermal measurements at 200 °C confirm the different kinetic behaviour of the MNLH-5tt and LCLH-tt samples. It can be seen in Fig. 7(b) that the MNLH-5tt sample desorbs about 5.5 wt% of hydrogen in 50 minutes while dehydrogenation is practically not detected for the $Li_4(NH_2)_3Cl$–3LiH mixture. After dehydrogenation at 200 °C, the final material is still a mixture of cubic and hexagonal $Li_4(NH_2)_3Cl$ phases (see Fig. S2†), while the MNLH-tt sample was completely dehydrogenated (see Fig. S2†). Further rehydrogenation of LCLH-tt at 200 °C under 6.0 MPa is undetectable. The progressive formation of $Li_4(NH_2)_3Cl$ in MNLH-5 sample does not seem to be caused by the temperature (see Fig. S3†), instead the main reason that promotes the increase of this phase would be the successive cycling (see Fig. 2(b)). There is a correlation between the amount of this phase and the hydrogen storage properties: the amount of $Li_4(NH_2)_3Cl$ phase increases with hydrogen cycling, while both dehydrogenation rate and hydrogen storage capacity decrease. Then, the formation of the $Li_4(NH_2)_3Cl$ as secondary phase during hydrogen cycling clearly affects the hydrogen storage capacity of $Mg(NH_2)_2$–2LiH–2LiCl composite by restricting the complete dehydrogenation of $Li_2Mg_2(NH_2)_3$ by $LiNH_2$ consumption.

Fig. 8 shows the dehydrogenation PCI curves for the MNLH-5tt and LCLH-tt samples. The hydrogen desorption capacities obtained were about 5.1 and 3.1 wt% for MNLH-5tt and LCLH-tt in comparison with 5.5 and 4.5 wt%, respectively, expected according to the stoichiometry. The equilibrium hydrogen pressure during dehydrogenation for MNLH-5tt at 200 °C is higher (~2000 kPa) than the corresponding to LCLH-tt at 225 °C (~40 kPa). The big difference in these equilibrium pressures explain why the dehydrogenation at 200 °C from $Mg(NH_2)_2$–2LiH–2LiCl is a viable reaction while it is a difficult process from $Li_4(NH_2)_3Cl$–3LiH. As minor amounts of $Li_4(NH_2)_3Cl$ are present in the MNLH-5tt sample, it is expected that it does not decompose at 200 °C as it is more stable than $Mg(NH_2)_2$. This observation agrees with the negative effect of $Li_4(NH_2)_3Cl$ observed on the dehydrogenation kinetics, the hydrogen storage capacity during cycling and the activation energy obtained for the as-milled sample.

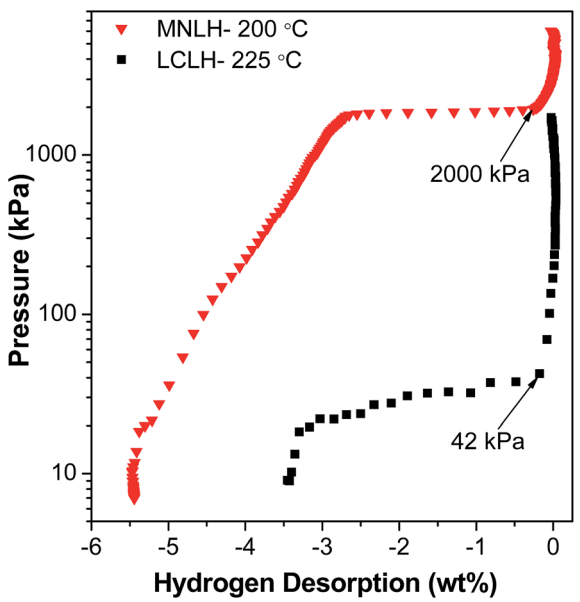

Fig. 8 Dehydrogenation PCI curves of $Mg(NH_2)_2$–2LiH–2LiCl at 200 °C and $Li_4(NH_2)_3Cl$–3LiH at 225 °C.

Regarding the dehydrogenation rates, although the amide-halide phases are known as promoters of lithium conductivity favouring dehydrogenation rates,[31,33] our experimental results suggest an opposite effect. A possible explanation is that the diffusion pathways between $Mg(NH_2)_2$ and LiH were hindered respect to the as-milled sample due to the formation of an additional phase even when this amide-chloride phase promotes the Li^+ mobility.

3.6 Reaction pathway of dehydrogenation

On the basis of the dehydrogenation studies and structural changes of $Mg(NH_2)_2$–2LiH–2LiCl at different stages of hydrogen cycling, it can be deduced that the presence of LiCl as a co-product changes the pathways for dehydrogenation. Firstly, $Li_4(NH_2)_3Cl$ is formed during thermal treatment up to 200 °C under 6.0 MPa of hydrogen storage (Fig. 3). The possible route of formation involves the presence of minor amounts of $LiNH_2$ due to uncompleted metathesis reaction (5) and LiCl:

$$3LiNH_2 + LiCl \rightarrow Li_4(NH_2)_3Cl \quad (6)$$

Secondly, the first step during $Mg(NH_2)_2$–2LiH–2LiCl dehydrogenation forms $LiNH_2$ and $Li_2Mg_2(NH)_3$ (see Fig. 2(b), first cycle). The reaction can be represented by reaction (2) and involves 4.4 wt% of hydrogen releasing:

$$2Mg(NH_2)_2 + 3LiH \leftrightarrow Li_2Mg_2(NH)_3 + LiNH_2 + 3H_2$$

Thirdly, $Li_2Mg_2(NH)_3$ could be completely dehydrogenated to obtain $Li_2Mg(NH)_2$ as a solid phase, according to reaction (3):

$$Li_2Mg_2(NH)_3 + LiNH_2 + LiH \leftrightarrow 2Li_2Mg(NH)_2 + H_2$$

The combination of reactions (2) and (3) constitute the traditional dehydrogenation pathway of $Mg(NH_2)_2$–2LiH. However, when reaction (2) occurs at 200 °C, the newly $LiNH_2$ formed could react with LiCl highly dispersed forming extra amount of $Li_4(NH_2)_3Cl$ according to reaction (6). Reactions (3) and (6) are competitive because both require $LiNH_2$ as a starting phase. The advance degree of each reaction depends on their relative reaction rates at the temperature and pressure selected. Reaction (6) could be faster than reaction (3) under the

conditions applied in this study and then $LiNH_2$ is mainly consumed to form $Li_4(NH_2)_3Cl$ during dehydrogenation. This result is supported by the fact that $LiNH_2$ has to react with only one solid specie (reaction (6)) instead of two solid species (reaction (2)), being the first case more probable.

Considering that $Li_4(NH_2)_3Cl$ is not dehydrogenated at 200 °C (Fig. 7(b), 8 and S2†) and that hydrogen cycling of $Mg(NH_2)_2$–2LiH–2LiCl sample could lead to the progressive formation of $Li_4(NH_2)_3Cl$ *via* reaction (6), the total hydrogen storage capacity of the system decreases. In addition, hydrogenation of $Li_2Mg_2(NH)_3$ through reaction (2) is limited as it requires $LiNH_2$. Therefore, the amount of $Li_2Mg_2(NH)_3$ in the hydrogenated state also increases with the cycling progress.

The kinetic and thermodynamic studies performed for the MNLH-5, MNLH-5tt and $Li_4(NH_2)_3Cl$–3LiH materials confirm the worst effect of the amide-chloride phase formation during hydrogen cycling in the $Mg(NH_2)_2$–2LiH–2LiCl composite. Clearly, the $Li_4(NH_2)_3Cl$ formation *via* $LiNH_2$ is the main responsible for the loss of capacity due to its stability. It is important to mention that the nanostructured $Mg(NH_2)_2$–2LiH–2LiCl composite prepared by metathesis reaction still has a good desorption kinetics and high storage capacity at 200 °C after the 8th cycle, constituting an interesting candidate for applications in hydrogen storage. The use of a different Mg precursor in the metathesis reaction (5) to avoid the formation of LiCl as dispersing phase is under exploration.

4. Conclusions

In this work, we investigated the dehydrogenation properties of the $Mg(NH_2)_2$–2LiH–2LiCl composite and the influence of LiCl on the structural, microstructural and thermal changes that occur during hydrogen cycling. The $Mg(NH_2)_2$ was synthesized by a metathesis reaction between $LiNH_2$ and $MgCl_2$ forming LiCl as a co-product. Next, LiH was added by milling to produce the $Mg(NH_2)_2$–2LiH–2LiCl composite. The presence of LiCl operates as a separation phase and favours the nanostructure of the composite.

The as-milled $Mg(NH_2)_2$–2LiH–2LiCl material shows good dehydrogenation rate and high hydrogen storage capacity at 200 °C. However, its hydrogen storage performance declines as a consequence of hydrogen cycling. The main reaction pathway during dehydrogenation follows the traditional mechanism involving the formation of $Li_2Mg_2(NH)_3$ plus $LiNH_2$ in the first step and $2Li_2Mg(NH)_2$ in the second step. In addition, another alternative reaction pathway is operational and involves $LiNH_2$ as reactive. The formation of $Li_4(NH_2)_3Cl$ from $LiNH_2$ and LiCl co-product is a competitive reaction with the complete dehydrogenation of $Li_2Mg_2(NH)_3$ plus $LiNH_2$ to produce $Li_2Mg(NH)_2$. In fact, after the first hydrogenation cycle, both $Li_2Mg_2(NH_2)_3$ and $Li_4(NH_2)_3Cl$ are clearly identified. Additional hydrogen cycling increases the relative amount of $Li_2Mg_2(NH_2)_3$ and $Li_4(NH_2)_3Cl$. The experimental evidence indicates that $LiNH_2$ formed *in situ* prefers to react with LiCl, which changes the reaction pathway. The activation energies of as-milled and as-cycled composites also demonstrate the negative effect of $Li_4(NH_2)_3Cl$ phase by an increment of 10 kJ mol^{-1} with respect to the value of the as-milled sample. No evidence of ammonia emission was detected at 200 °C.

Acknowledgements

This study has been partially supported by CONICET (National Council of Scientific and Technological Research), CNEA (National Commission of Atomic Energy), ANPCyT (PICT No. 1052) and Instituto Balseiro (University of Cuyo). The authors would like to thank the Department of Characterization of Materials (CNEA) for the use of XRD and SEM devices.

References

1 B. Bogdanović and M. Schwickardi, *J. Alloys Compd.*, 1997, **253**, 1.
2 W. Luo, *J. Alloys Compd.*, 2004, **381**, 284.
3 Z. Xiong, G. T. Wu, J. J. Hu and P. Chen, *Adv. Mater.*, 2004, **16**, 1522.
4 H.-W. Li, Y. Yan, S. Orimo, A. Züttel and C. M. Jensen, *Energies*, 2011, **4**, 185.
5 P. Chen, Z. Xiong, J. Luo, J. Lin and K. L. Tan, *Nature*, 2002, **420**, 302.
6 P. Chen, Z. Xiong, J. Luo, J. Lin and K. L. Tan, *J. Phys. Chem. B*, 2003, **107**, 10967.
7 Y. Kojima and Y. Kawai, *J. Alloys Compd.*, 2005, **395**, 236.
8 S. Isobe, T. Ichikawa, K. Tokoyoda, N. Hanada, H. Leng, H. Fujii and Y. Kojima, *Thermochim. Acta*, 2008, **468**, 35.
9 S. V. Alapati, J. K. Johnson and D. S. Sholl, *J. Phys. Chem. B*, 2006, **110**, 8769.
10 J. J. Vajo and G. L. Olson, *Scr. Mater.*, 2007, **56**, 829.
11 H. Y. Leng, T. Ichikawa, S. Isobe, S. Hino, N. Hanada and H. Fujii, *J. Alloys Compd.*, 2005, **404–406**, 443.
12 Y. Liu, J. Hu, Z. Xiong and G. Wu, *J. Mater. Res.*, 2007, **22**, 1339.
13 J. Hu and M. Fichtner, *Chem. Mater.*, 2009, **21**, 3485.
14 R. R. Shahi, H. Raghubanshi, M. A. Shaz and O. N. Srivastava, *Int. J. Hydrogen Energy*, 2013, **38**, 8863.
15 H. Pan, S. Shi, Y. Liu, B. Li, Y. Yang and M. Gao, *Dalton Trans.*, 2013, **42**, 3802.
16 B. Zhang and Y. Wu, *J. Alloys Compd.*, 2014, **613**, 199.
17 Z. Xiong, J. Hu, G. Wu, P. Chen, W. Luo, K. Gross and J. Wang, *J. Alloys Compd.*, 2005, **398**, 235.
18 Y. Nakamori, G. Kitahara and S. Orimo, *J. Power Sources*, 2004, **138**, 309.
19 J. Hu and M. Fichtner, *Chem. Mater.*, 2009, **21**, 348.
20 P. Chen, Z. Xiong, L. Yang, G. Wu and W. Luo, *J. Phys. Chem. B*, 2006, **110**, 14221.
21 J. Hu, Y. Liu, G. Wu, Z. Xiong and P. Chen, *J. Phys. Chem. C*, 2007, **111**, 18439–18443.
22 T. Markmaitree and L. L. Shaw, *J. Power Sources*, 2010, **195**, 1984.
23 Y. Liu, K. Zhong, K. Luo, M. Gao, H. Pan and Q. Wang, *J. Am. Chem. Soc.*, 2009, **131**, 1862.
24 L. Xie, Y. Liu, G. Li and X. Li, *J. Phys. Chem. C*, 2009, **113**, 14523.

25 J. Huot, D. B. Ravnsbæk, J. Zhang, F. Cuevas, M. Latroche and T. R. Jensen, *Prog. Mater. Sci.*, 2013, **58**, 30–75.
26 J. Wang, P. Chen, H. Pan, Z. Xiong, M. Gao, G. Wu, C. Liang, C. Li, B. Li and J. Wang, *ChemSusChem*, 2013, **6**, 2181–2189.
27 C. Liang, Y. F. Liu, M. X. Gao and H. G. Pan, *J. Mater. Chem. A*, 2013, **1**, 5031.
28 B.-X. Dong, J. Ge, Y.-L. Teng, J.-J. Gao and L. Song, *J. Mater. Chem. A*, 2015, **3**, 905.
29 Y. Liu, C. Li, B. Li, M. Gao and H. Pan, *J. Phys. Chem. C*, 2013, **117**, 866.
30 H. Leng, Z. Wua, W. Duan, G. Xia and Z. Li, *Int. J. Hydrogen Energy*, 2012, **37**, 903.
31 P. A. Anderson, P. A. Chater, D. R. Hewett and P. R. Slater, *Faraday Discuss.*, 2011, **151**, 271.
32 C. Price, J. Gray, R. Lascola Jr and D. L. Anton, *Int. J. Hydrogen Energy*, 2012, **37**, 2742.
33 B. Li, Y. Liu, C. Li, M. Gao and H. Pan, *J. Mater. Chem. A*, 2014, **2**, 3155.
34 H. Cao, H. Wang, T. He, G. Wu, Z. Xiong, J. Qiu and P. Chen, *RSC Adv.*, 2014, **4**, 32555.
35 R. A. Davies, D. R. Hewett and P. A. Anderson, *Adv. Nat. Sci.: Nanosci. Nanotechnol.*, 2015, **6**, 015005.
36 R. A. Davies and P. A. Anderson, *Int. J. Hydrogen Energy*, 2015, **40**, 3001.
37 L. Fernández Albanesi, P. Arneodo Larochette and F. C. Gennari, *Int. J. Hydrogen Energy*, 2013, **38**, 12325.
38 H. E. Kissinger, *Anal. Chem.*, 1957, **29**, 1702.
39 G. von Linde and R. Juza, *Z. Anorg. Allg. Chem.*, 1974, **409**, 199.
40 D. A. Sheppard, M. Paskevicius and C. E. Buckley, *J. Alloys Compd.*, 2010, **492**, L72.
41 H. Cao, G. Wu, Y. Zhang, Z. Xiong, J. Qiu and P. Chen, *J. Mater. Chem. A*, 2014, **2**, 15816.
42 C. Liang, M. Gao, H. Pan, Y. Liu and M. Yan, *Int. J. Hydrogen Energy*, 2014, **39**, 17754.
43 E. Weidner, F. Dolci, J. Hu, W. Lohstroh, T. Hansen, D. J. Bull and M. Fichtner, *J. Phys. Chem. C*, 2009, **113**, 15772.
44 F. C. Gennari, *Int. J. Hydrogen Energy*, 2012, **37**, 18895.